Journal of The Electrochemical Society, **155** (12) A986-A994 (2008)
0013-4651/2008/155(12)/A986/9/$23.00 © The Electrochemical Society

An Electrical Circuit for Modeling the Dynamic Response of Li-Ion Polymer Batteries

P. L. Moss,[a] G. Au,[b] E. J. Plichta,[b] and J. P. Zheng[a,c,*,z]

[a]*Department of Electrical and Computer Engineering, Florida A&M University and Florida State University, Tallahassee, Florida 32310, USA*
[b]*US Army Power Division, Army CERDEC, Ft. Monmouth, New Jersey 07703, USA*
[c]*Center for Advanced Power Systems, Florida State University, Tallahassee, Florida 32310, USA*

An equivalent electrical circuit model based on parameters taken from ac impedance measurements obtained from a Li-ion polymer battery is simulated in a Matlab/Simulink environment. The model representation contains relevant parameters, including ohmic resistance, slow migration of Li-ions through the surface layers, faradaic charge transfer process, solid-state diffusion of Li-ions, and charge accumulation (intercalation capacitance) within the host material. The model also takes into account the non-homogeneous distribution properties (e.g, particle size, pore geometry) of the electrode which account for deviation from the ideal finite space Warburg behavior. The simulated and experimental results are compared and demonstrate that the impedance model can accurately predict the discharge power performance and transient and dynamic behavior of the Li-ion polymer batteries.
 [DOI: 10.1149/1.2999375]

Manuscript submitted June 6, 2008; revised manuscript received September 18, 2008. Published October 21, 2008.

The increased demand for the limited available fossil fuels and increasing environmental concerns have spurred worldwide interest in the use of alternative energy and storage systems, particularly for electric and hybrid-electric vehicle applications.[1,2] Because of safety issues and the wide variety of shapes and sizes required for various applications, much attention has been focused on research and development of advanced lithium-ion and lithium-ion polymer systems, which can deliver increased energy and power densities.[3-6] The optimization of battery performance is determined by various material properties; therefore, modeling the effects of transport properties on electrochemical performance can result in improved cell design, reduced testing time, and accurate modeling of battery behavior, which is required for embedded power systems.[7] One of the primary challenges is the development of simple electrochemical models that are cost effective and can accurately predict important battery parameters (i.e., mechanisms that contribute to aging, battery run-time, power response, and energy consumption). These parameters are critical to cell efficiency and can easily be implemented in circuit-based simulator programs (e.g., Pspice, electronic workbench) for prototype evaluation and hardware optimization.

The galvanostatic charge discharge behavior of lithium-ion batteries was modeled by Doyle et al.[8] using concentration solution theory, which uses a mathematical model to describe lithium-ion transport in three regions of operation. These regions include transport in solution, and the two solid phases of the composite electrodes for which boundary conditions are applied. Their mathematical model accurately describes the charge–discharge behavior of the electrochemical cell. However, this model requires a detailed understanding of the complex physical and chemical processes, which may not be available or may not be understood by an electrical engineer.[9] Additionally, to many engineers these equations present additional complexities that may increase simulation time.

A time domain model mapped from impedance data in the frequency domain was developed by Buller et al.,[10] which accurately modeled the dynamic behavior of an electrochemical capacitor and a lithium-ion battery. However, for these models nonlinear distribution properties in the low-frequency portion of the impedance spectrum and battery run-time is not considered. These circuit-based models are very useful and simple because they allow the complex electrochemical process to be replaced by a simple electrical circuit, which correlates well with battery dynamics.

The current model takes into account the nonhomogeneous distribution properties of diffusion, including the nonlinear response to current magnitude and direction (i.e., positive and negative currents). The proposed model also includes an accurate representation of the dc nonlinear behavior in addition to the dynamic and transient response of the electrochemical cell under various load conditions. Additionally, similar techniques[11] proposed in previous work were used to elucidate the power and energy performance of an electrochemical double-layer capacitor (EDLC). The model involves the mapping of the impedance spectra from the frequency domain to the time domain for the EDLC. A nonlinear circuit, which includes resistors, capacitors, inductors, and nonlinear electrical components, were used to describe the cell at various equilibrium points. In this work, we focused our attention on modeling the performance of a lithium-ion polymer battery manufactured by Sony Corporation. This cell has a typical electrode structure Li_xC_6 as negative electrode and $Li_{1-x}CoO_2$ as positive electrode material.

Experimental

The battery used in this experiment was a commercial Li-ion polymer battery with a nominal capacity of 800 mAh (UP383562A, Sony Co.). To determine the equivalent circuit for this battery, electrochemical impedance (EIS) measurements were carried out at various states of charge (SOC) using a Solartron 1250B frequency response analyzer controlled by Zplot and Corrware software (Scribner Associated). Additionally, positive charge and negative discharge currents were used to elucidate the dependency of charge transfer resistance R_{ct} on dc charge and discharge currents. The frequency spectrum for this current work was limited to frequencies in the range of 20 kHz to 1 mHz, operating in galvanostatic mode with a signal amplitude of 100 mA and dc current I_{dc} from +0.8 to –0.8 A in increments of 0.1 A. Additionally, impedance spectra were recorded in the bias potential window from 4.15 to 3.0 V, in increments of 0.2 V. Impedance measurements were conducted only after the dc potential had a 6 h stabilization period at 25°C.

For constant dc current discharge measurements, the cell was charged at a constant current of 0.5 A until the voltage reached 4.15 V, then shifted to constant voltage charge mode until the current decayed to 50 mA. The cell was then discharged at 1 C (800 mA), 3 C/4 (600 mA), C/4 (200 mA), C/10 (80 mA) to 3.0 V (100% DOD). Pulse charge–discharge was also conducted at 94% SOC using constant step pulses (0.6 A, 1 s), (−0.1 A, 1 s), (−1 A, 1 s), (0.5 A, 1 s) for a duration of 4 s and repeated for 20 s. DC charge/discharge and pulse studies were all carried out at ambient temperature on an Arbin BT2000 battery test system.

After collecting the experimental impedance spectrum, the various processes were fitted to an equivalent circuit using the frequency limits from the experiment. The model was then validated by comparing the simulated and experimental voltage profiles for several current pulse profiles.

* Electrochemical Society Active Member.
[z] E-mail: zheng@eng.fsu.edu

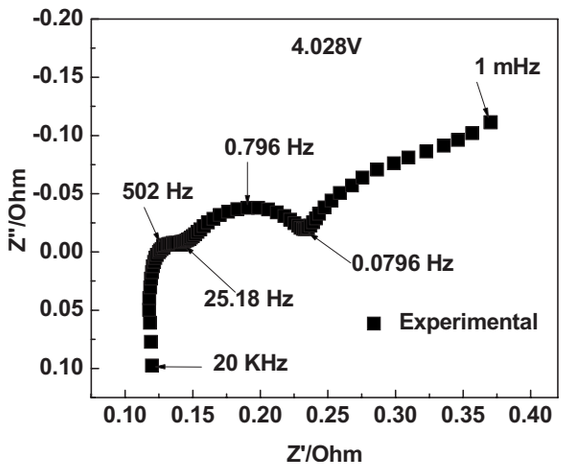

Figure 1. Impedance spectrum for Li-ion polymer battery (Sony UP383562A) at an OCP of 4.0 V (I_{dc} = 0,84.3% SOC).

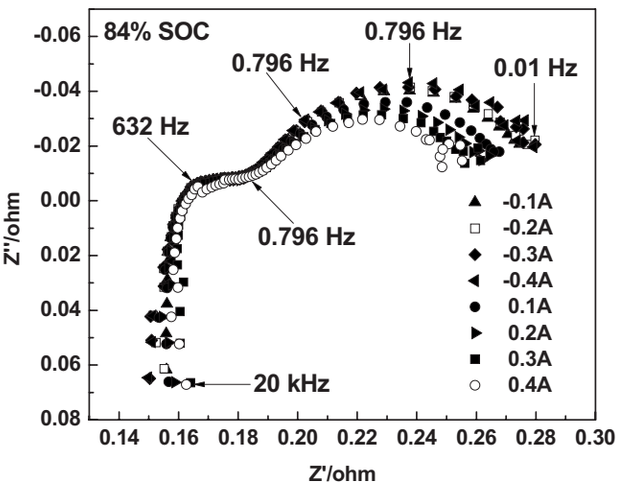

Figure 2. Impedance spectra as a function of dc charge and discharge current at 84% SOC.

Results and Discussion

Impedance response of Li-ion polymer battery.— Figure 1 shows the result of the typical impedance spectra taken at 4.0 V (84% SOC) for a fresh commercial polymer cell, where Z' and Z'' are the real and imaginary impedance response of the battery, respectively. The impedance spectra comprised an inductive tail at high frequencies, which is attributed to the porosity of the electrode jelly-roll structure and connection leads of the battery,[12,13] the high-frequency intercept ($\sim$1.262 kHz) on the real axis represents the total ohmic resistance ($\sim$0.12 Ω) of the cell, which includes the electrolyte resistance, contact resistance, electronic contacts, etc.; depressed semicircles at middle to high frequencies (25.18–502 Hz) can be ascribed to the solid electrolyte interface layer of the electrodes (at the film electrode/solution interface); the semicircle in the mid-frequency (0.0796–25.18 Hz) range is characteristic of the charge-transfer kinetics at the electrode/electrolyte interface,[14,15] the low-frequency (0.0796 Hz to 1 mHz) portion of the impedance can be assigned to the solid-state Warburg diffusion of lithium ions into the porous electrode matrix. At extremely low frequencies ($C_{int} = -1/\omega Z''$, $\omega \rightarrow 0$) the impedance response is associated with the differential intercalation capacitance of the electrode, which describes the accumulation of lithium ions within the host material.[16]

To investigate the nonlinear dependency of impedance at different dc charging and discharging currents (I_{dc}), the complex impedance spectra shown in Fig. 2 were collected at 84% SOC in the frequency range of 20 kHz to 0.01 Hz. The part of the impedance spectrum in the frequency range of 20 kHz to 0.796 Hz shows little variation with current magnitude and direction, therefore, *R-C* circuit elements used to model this portion of the impedance spectrum can be considered constant. It can also be observed that the charge-transfer resistance is strongly dependent on the magnitude of charge and discharge currents. The nonlinear change in the charge transfer resistance slowly increased with increasing negative discharge currents and decreased with positive charge currents. For low charge and discharge currents ($<$0.5 C), a $<$2% deviation in the open-circuit potential (OCP) was observed between measurements; however, the SOC was adjusted to 84% for consecutive measurement due to larger deviations that would be observed for higher charge and discharge currents.

Equivalent circuit modeling and parameter estimation.— The charge-transfer kinetic reaction between an ionic and an electronic conductor is inherently slow and can only proceed at an accelerated rate when the potential energy barrier between the two conductors has been overcome by the reaction species.[17] This potential barrier is termed *activation polarization* and is the rate-limiting step for charge transfer between the electronic and ionic conductor. Generally, the relationship between the current density, the faradiac exchange current density, and the electrode surface over potential η can be described by the Butler–Volmer equation, which is given by[18]

$$i = i_0\left[\exp\left(\frac{n\alpha F}{RT}\eta\right) - \exp\left(-\frac{n(1-\alpha)F}{RT}\eta\right)\right] \quad [1]$$

Here, i is the current density, i_0 is the exchange current density, α is the charge transfer coefficient, n is the number of electrons per molecule reduced or oxidized, F is Faraday's constant, R is the gas constant, and T is the absolute temperature in Kelvin. The two exponential terms on the right-hand side of Eq. 1 represent the forward and reverse electrode reaction process, respectively. At equilibrium potentials, the exchange current density is the current exchanged between the ionic and electronic conductor.[19]

The typical nonlinear dependency of faradaic charge transfer resistance R_{ct} on current (i.e., positive and negative) was observed in the impedance spectra in Fig. 2. The charge-transfer resistance at the electrode-electrolyte interface can then be determined by differentiating Eq. 1 and taking its reciprocal, which result in the following equation

$$R_{ct}^{-1}(\eta) = \frac{di}{d\eta} = \frac{i_0 nF}{RT}\left[\alpha\exp\left(\frac{n\alpha F}{RT}\eta\right) + (1-\alpha)\times\exp\left(-\frac{n(1-\alpha)F}{RT}\eta\right)\right] \quad [2]$$

$$R_{ct}^{-1} \approx \frac{RT}{i_0 nF} \quad [3]$$

When the activation over potential is a few millivolts, Eq. 2 can be approximated by Eq. 3. The value of i_0 and its variation with SOC can then be calculated using Eq. 3. Similarly, the Warburg diffusive behavior that is usually observed in the low-frequency portion of the impedance spectra with a 45° incline can be represented by a transmission line model having a value given by the finite-space Warburg (FSW) element[20]

$$Z_W = R_W\frac{\coth\sqrt{i\omega\tau_d}}{\sqrt{i\omega\tau_d}} \quad [4]$$

Here, R_w is the effective distributed ionic impedance of the electrodes, τ_d is the diffusion time constant, and ω is the angular frequency. Assuming uniform distributed double-layer capacitance be-

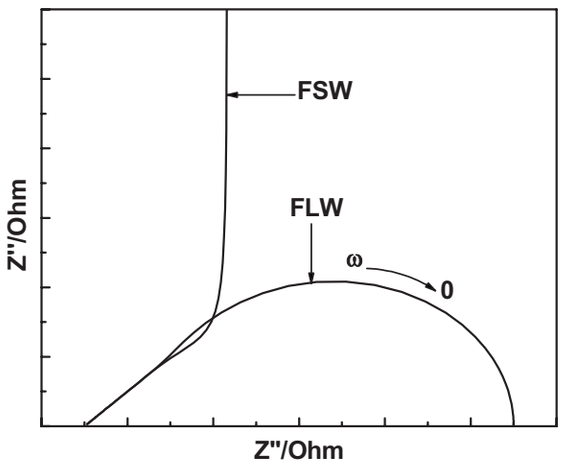

Figure 3. Typical impedance response of FSW and FLW elements.

havior along the inner wall of a cylindrical pore, then the classical 45° Warburg-type response in the complex plane would be observed.[21,22] However, the low-frequency portion of the impedance spectra in the complex plane (Fig. 1) cannot adequately be modeled using the classical FSW impedance element given by Eq. 4. The nonlinear impedance response observed in the complex plane at low frequencies is believed to be due to the nonuniform distribution properties of the electrodes, which include particle size, pore size, shape (pore geometry), etc.[23-26]

To more accurately model the low-frequency portion of the impedance spectra (which consists of nonuniform solid-state diffusion of Li^+ under finite transmission lines condition with reflective boundary conditions), we adopted the equivalent circuit proposed by Levi et al.[23] which consists of the finite length Warburg (FLW) element in series with intercalation capacitance, C_{int}. The governing equation for the FLW element can be expressed in terms of the distributed impedance of a transmission line containing three parameters with well-defined physical meaning and is given by[27]

$$Z_W = R_W \frac{\tanh(\sqrt{j\omega\tau_d})}{\sqrt{j\omega\tau_d}} \quad [5]$$

Here, R_w is the ionic impedance of the porous electrode, $\tau_d = \ell^2/D$ is the diffusion time constant with D as the diffusion coefficient, ℓ is the length of the diffusion region in the electrode, and ω (in radians per second) is the angular frequency. The major difference between the FSW and the FLW element is that the latter resembles a resistor at low frequencies and the former a capacitor as shown in Fig. 3.

Figure 4 shows the equivalent circuit used to fit the ac impedance spectra recorded at a range of potential voltages from 3.42 to 4.15 V (measurements were taken at OCP after a 6 h rest period) shown in Fig. 5. The impedance of the porous electrodes can be represented by a modified Randles equivalent circuit that contains series resistance R_s, which represents the ohmic resistance of the battery, including the electrolyte, electronic contacts, particle-to-particle contact resistance, etc.; R_n and C_n describe the slow migration of Li^+ through the surface films;[14,15,23,28,29] R_{ct} and C_{dl} represent the faradaic charge transfer resistance and double-layer capacitance of the electrodes, respectively. The solid-state diffusion of Li^+ is described by the FLW element, while the accumulation of Li^+ within the electrode matrix is described by the intercalation capacitance C_{int}. The effective impedances, including charge transfer resistance R_{ct} and diffusion impedance Z_W of the anode and cathode, cannot be separated and resolved into their individual spectra; therefore, their impedances are lumped together to effectively represent the total impedance of the electrochemical cell.[30]

The optimum parameters in the circuit were determined by the method of nonlinear least square (NLLS) fitting procedure. The use of the intercalation capacitance C_{int} in the model takes into account the accumulation and depletion of Li^+, which results in the variation of OCP with SOC. The Warburg diffusion impedance in the complex plane occurs with a distinguishable and nonoverlapping time constant; therefore, the Warburg impedance in this model can be placed in series with the parallel faradaic charge transfer resistance and double-layer capacitance. From the experimental impedance spectra shown in Fig. 5a-d, good agreement can be observed over a wide range of frequencies and SOC.

The dependency of R_{ct} on I_{dc} and SOC is shown in Fig. 6 for the experimental (symbol) and simulated (solid line) values of charge transfer resistance. Equation 2 was used to estimate the charge transfer resistance as a function of charge and discharge currents. The simulated curves were constructed using parameters arbitrarily assigned similar to those in Ref. 20, (i.e., $\alpha = 0.64$, $n = 0.62$, and i_0 a function of SOC). The results showed that Eq. 2 can be used with great accuracy to calculate R_{ct}. In Table I, a minor dependency on SOC is observed for ohmic resistance R_s, surface film resistance (R_{f1}, R_{f2}, R_{f3}), and capacitance (C_{f1}, C_{f2}, C_{f3}).

The optimum values of the complete impedance parameters at various SOC (99, 87.85, 59.78, 7.31, 2.88, and 1.33%) and $I_{dc} = 0$ are summarized in Table I. The results showed that the elements are SOC dependent; however, the charge transfer resistance showed the most significant dependency on SOC. It should also be noted that the ohmic resistance R_s and double-layer capacitance C_{dl} showed minimal variation with the state of charge.

The experimental data points for each circuit element in Table I can be estimated by inserting these parameter values into a lookup table. Equations obtained from fitting that relate the continuous charge in magnitude of each element to the change in battery state of charge can also be used. These equations can then be used in a numerical simulator to represent the polarization impedance for mass and charge transport processes. In this particular experiment, the latter was chosen. The change in magnitude for each element

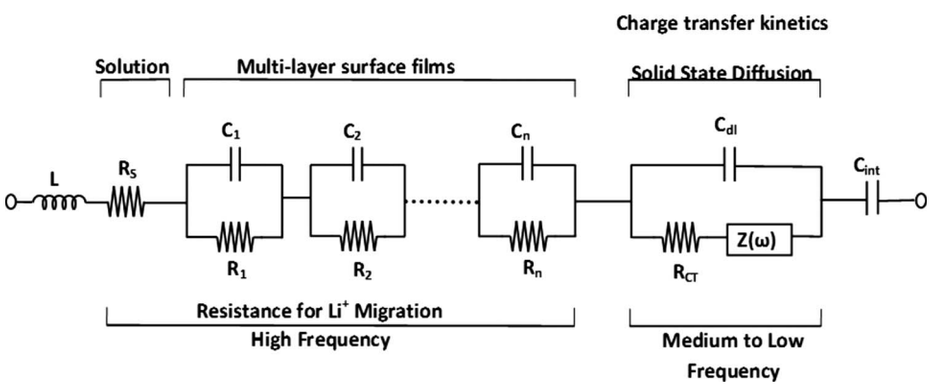

Figure 4. Equivalent circuit used to model impedance spectra.

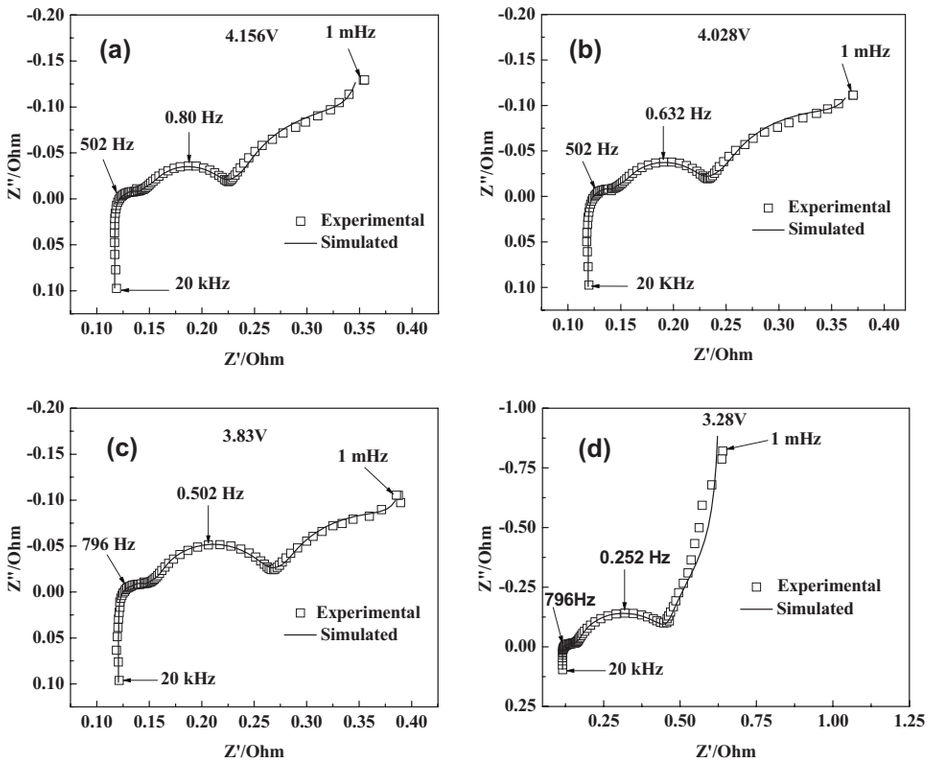

Figure 5. (a–d) Impedance at various OCPs. Impedance was simulated using the circuit from Fig. 4 in the frequency range of 20 kHz to 1 mHz.

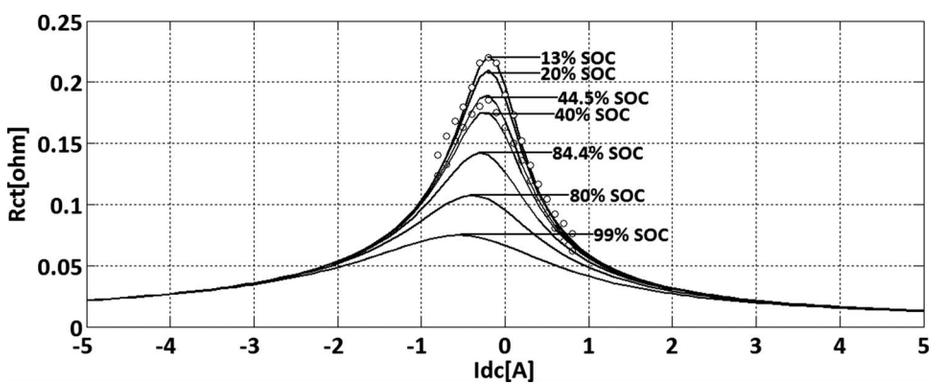

Figure 6. Comparison between experimental (symbol) and simulated (line) change in charge transfer resistance R_{ct} at 13, 45, and 84% SOC (25°C) for various charge–discharge currents.

Table I. Fitted parameters with state-of-charge variation at $I_{dc} = 0$.

SOC (%)	99	87.85	59.78	7.31	2.88	1.33
L (μH)	0.7769	0.7926	0.78722	0.49685	0.50253	0.75653
R_s (mΩ)	116.96	119.07	120.56	82.074	88.106	115.53
R_{f1} (mΩ)	10.498	10.498	13.122	14.998	15.596	17.111
R_{f2} (mΩ)	13.015	13.015	14.02	17.92	19.874	22.412
R_{f3} (mΩ)	12.759	12.759	11.785	15.654	16.279	19.096
C_{f1} (mF)	12.593	12.593	11.672	8.2548	8.4584	10.447
C_{f2} (mF)	93.656	93.656	105.74	98.663	96.163	123.04
C_{f3} (F)	1.361	1.361	1.421	1.989	1.699	1.996
C_{dl} (F)	2.700	2.624	2.528	2.635	2.578	2.576
R_{ct} (mΩ)	63.236	67.766	97.347	211.30	237.44	258.38
R_w (mΩ)	139.67	152.19	138.03	165.51	157.98	204.79
T (s)	120.7	129	124.9	110.9	103.5	118.3
P	0.5	0.5	0.5	0.5	0.5	0.5
C_{int} (F)	1669	2269	2429	613.4	319	191.3

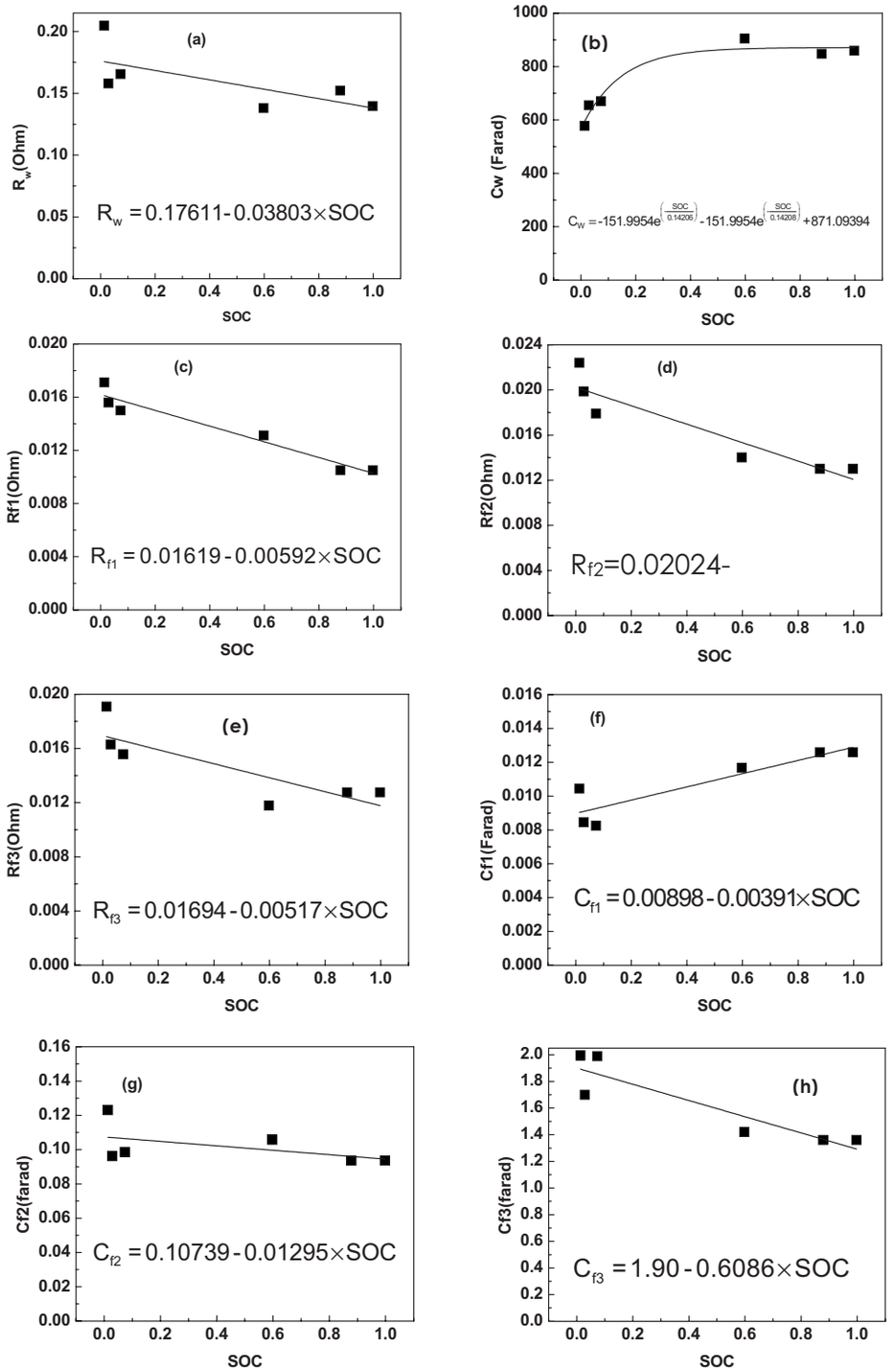

Figure 7. Estimate of change in circuit parameters with SOC.

with state of charge in addition to linear and nonlinear curve fitting is shown in Fig. 7a-h. The solid line represents the estimated change in magnitude of parameters with SOC using the inserted equations; the observed plots from fitting are closely matched to the discrete experimental data points obtained from impedance measurements. It should be noted that all simulations, including cell voltage vs SOC, pulse response, and Ragone plot, are dependent on parameters that are extracted from impedance spectra, which are SOC dependent; however, the charge transfer resistance R_{ct}, not only depends on SOC but also on the current magnitude and direction. Therefore, it is omitted from Fig. 8-13. Parameters with minimal SOC dependency can be set to constant values during charge–discharge simulations.

Transmission line model Li–ion polymer battery.— According to our previous analysis, the FLW element is a suitable approach to describe the low-frequency portion of the impedance spectra, which consists of solid-state diffusion of lithium-ions and charge accumulation in the electrode matrix at low frequencies. To illustrate the use of this impedance model in real-time applications requires a time-

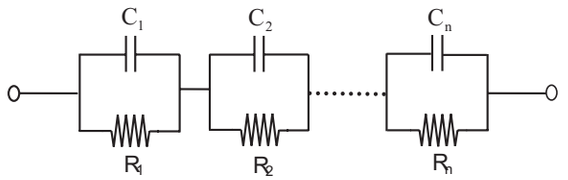

Figure 8. Parallel *R-C* circuit used to approximate solid-state Warburg diffusion.

domain representation of the impedance spectra in the frequency domain. According to Ref. 27, the impulse response of the Warburg impedance from Eq. 5 is given by

$$\frac{k_2}{\sqrt{j\omega}}\tanh\left(\frac{k_1}{k_2}\sqrt{j\omega}\right)\cdot - o\frac{2k_2^2}{k_1}\sum_{n=1}^{\infty}\exp\left(\frac{(2n-1)^2\pi^2k_2^2}{4k_1^2}t\right) \quad [6]$$

Comparing the parameters on the left-hand side of Eq. 6 to Eq. 5 leads to constant values for k_1 and k_2

$$k_1 = \frac{\tau}{C_W} = R_W \quad [7]$$

$$k_2 = \frac{\sqrt{\tau}}{C_W} = \sqrt{\frac{R_W}{C_W}} \quad [8]$$

The impulse response for a simple parallel *R-C* circuit shown in Eq. 9 has the same characteristic response as that of Eq. 6. Therefore, from the comparison of the two equations it is possible to represent the Warburg impedance as a series combination of parallel connected *R-C* circuit elements

$$\frac{1/C}{j\omega + 1/RC}\cdot - o\frac{1}{C}\exp\left(\frac{-t}{RC}\right) \quad [9]$$

Comparing the constants in Eq. 9 with those in Eq. 6 lead to values for the resistors and capacitors in the parallel *R-C* network, which is given by

$$C_n = \frac{k_1}{2k_2^2} \quad [10]$$

$$R_n = \frac{8k_1}{(2n-1)^2\pi^2} \quad [11]$$

The equivalent *R-C* circuit that can describe lithium-ion diffusion is depicted in Fig. 8. The discrete components are distributed over the length of the network. The more capacitor resistor pairs that are added to the network, the higher the order of accuracy in the dynamic response. The equation that describes the voltage behavior across each parallel *R-C* network is given by

$$v_n(t) = I_L R_n(1 - e^{-t/R_nC_n}) \quad [12]$$

Figure 9 presents the complete representation of the electrochemical system using discrete nonlinear electrical components. The equilibrium potential $U_0[V]$ is modeled by a SOC-dependent voltage source that depends on the availability of active material or energy

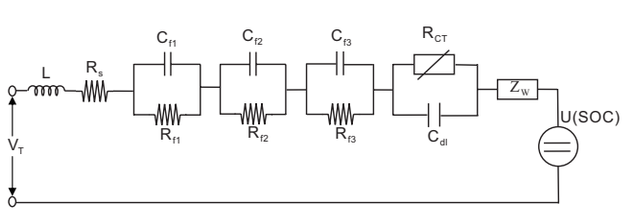

Figure 9. Schematic representation of lithium polymer battery derived from impedance response.

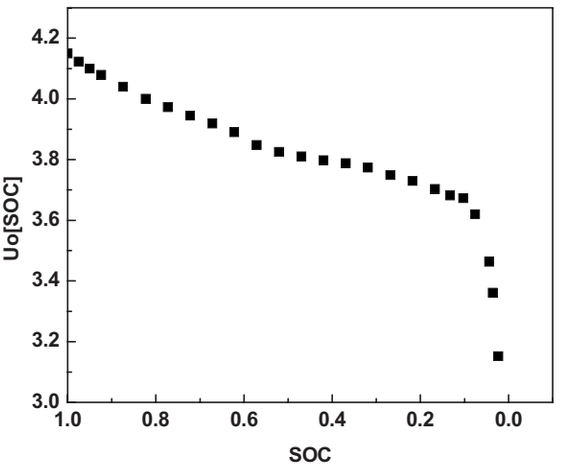

Figure 10. Dependency of OCV on SOC.

stored in the electrodes.[31] This dependent voltage source can be determined by charging the cell to various SOC, then after a rest period of 6 h, fixed values of the OCP are stored in a look-up table.[20] The disadvantage of using this method for SOC estimation is that it can be time consuming and dependent on other factors (e.g., temperature, age, pressure, and history of operating point). However, these additional dependent factors are not considered in this model. For this experiment, the OCV shown in Fig. 10 was determined experimentally at an operating point after a rest period of 6 h using constant current-constant voltage charge protocol and a cutoff current of 50 mA.

Equation 13 shows one common technique employed to estimate SOC. This simple technique, better known as columbic counting (i.e., current integration), relates the charge or current drawn from the cell to the OCP of the cell. The charge consumed during charge–discharge is a direct indictor of remaining SOC and is given by[32]

$$\mathrm{SOC}(T) = 1 - \frac{1}{3600Q_0}\int_0^T i(t)dt - \mathrm{SOC}(0) \quad [13]$$

Here, $i(t)$ is the charging/discharging current, SOC(0) is the initial state of charge of the battery, and Q_0 is the nominal capacity of the battery with SOC $\leqslant$ 1. The battery is considered fully charged when SOC(T) = 1, which in this case corresponds to an OCP of 4.17 V.

The dynamic response to arbitrary load currents can be described by the equivalent circuit in Fig. 9. In this equivalent circuit, *R-C* circuit elements describe the depressed semicircles observed at high- to mid-frequency (632–0.796 Hz) in the impedance spectra. Using the method of the NLLS procedure, three *R-C* circuit elements were found to be adequate for approximating this part of the impedance spectrum. The terminal voltage can then be described by

$$V_T = U_0[\mathrm{SOC}(t)] - i_L R_s - \sum_3 V_{fn} - L\frac{di_L}{dt} - R_{ct}i_L(1 - e^{-t/R_{ct}C_{dl}}) - V_w \quad [14]$$

Here, $U_0[\mathrm{SOC}(t)]$ is the OCP of the battery, V_{fn} is the voltage drop associated with surface films at the electrode-electrolyte interface, and V_w is the voltage drop ascribed to the slow Warburg diffusion process. The effect of the inductor voltage on the model is minimal because only pulse current or constant current charge–discharge is used in this model, which will result in an inductor voltage zero.

Model evaluation using Matlab/Simulink.— To investigate the validity of the present model under constant current discharge and pulse load (i.e., charge–discharge) conditions, the model was implemented in numerical simulator Matlab/Simulink. We applied several

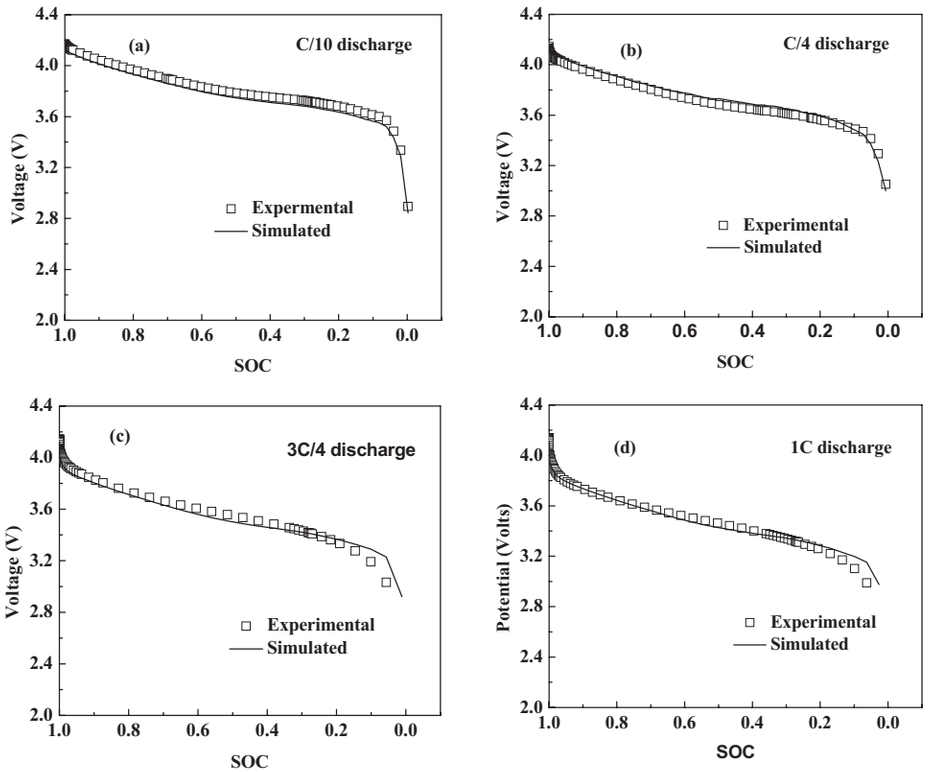

Figure 11. Comparison between simulated and experimental battery voltage response for several discharge currents: (a) C/10, (b) C/4, (c) 3 C/4, and (d) 1 C.

discharge currents (C/10, C/4, 3 C/4, 1 C) at 100% SOC (fully charged, ~4.15 V) to the model until it reached a cutoff voltage of 3.0 V. Figures 11a-d show the comparison between the experimental and simulated cell potential. The following characteristics were observed; at high and low discharge rates, a steep voltage drop is observed reflecting the ohmic polarization of the cell, an almost linear region reflecting additional overvoltages (i.e., activation overpotential and concentration overpotential), followed by a very steep slope at the end of discharge, which reflects the depletion in the available active material. The simulated terminal voltage in response to current demands agrees accurately with the experimental result at high and low discharge rates.

In order to confirm the validity of the impedance model to large current pulse applications, step current profile (0.6 A,1 s) to (−0.1 A,1 s) to (−1 A,1 s) to (0.5 A,1 s) was applied to the test cell at 94% SOC. The experimental and simulated voltage in response to step profile during a 20 s time duration is depicted in Fig. 12. In this range, the experimental voltage varied from a maximum value of 4.15 V to a minimum value of 3.78 V. In addition, a maximum error of 1.9% between the experimental and simulated terminal voltage was observed. It can be observed that the experimental terminal voltage and simulated voltage response show relatively accurate agreement.

Power performance of Li-ion polymer batteries.— An important parameter for energy storage devices (ESDs) in various appli-

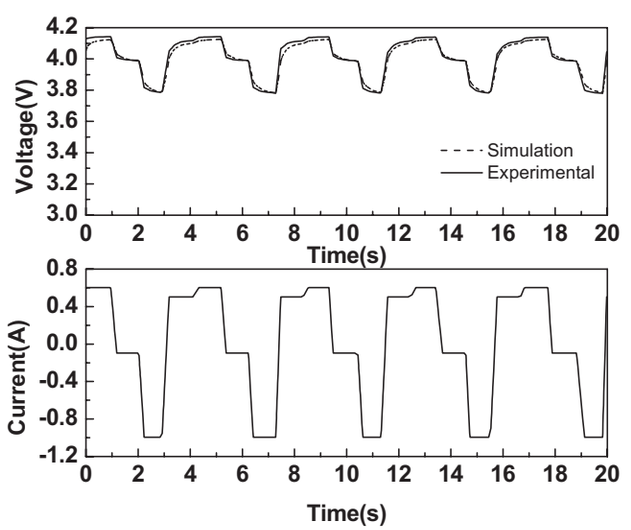

Figure 12. Comparison between simulated and experimental battery voltage in response to applied current pulse.

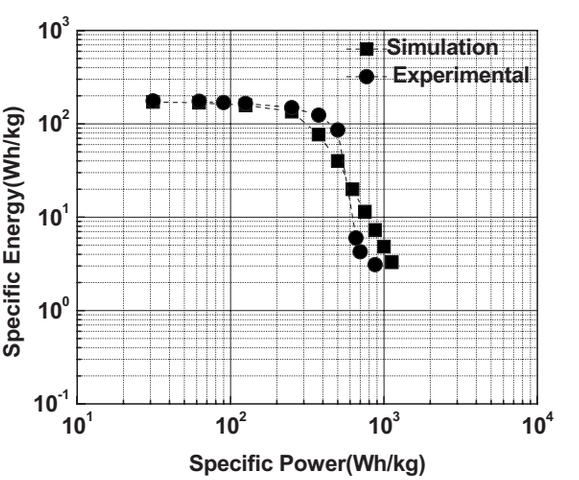

Figure 13. Computer simulation of Ragone plot for Sony UP383562A LIP cell.

cations includes the optimization of energy and power densities. In addition to increased pulse power demands in digital communication devices and in hybrid electric vehicle applications, batteries are expected to have increased energy density capability. One method for comparing the battery capability to deliver both maximum power and energy is to use Ragone plots, which are displayed on a log-log plane, the relationship between power and energy densities. From these plots, the optimum working point can be determined, which indicates where the power density (i.e., fast discharge) and energy densities (i.e., slow discharge) are highest.[33] Computer simulation can be a powerful tool for modeling Ragone plots for which comparative analysis (e.g., performance) can be made between various batteries.[34] This can prove to be an efficient and effective method for choosing a battery for an application-specific design.

For an ideal battery (i.e., without leakage) the energy delivered to a load can be described by[33]

$$E = \frac{2R_S Q_0 P}{U_0 - \sqrt{U_0^2 - 4R_S P}} \quad [15]$$

Here, U_0 is the battery voltage, R_s is the ohmic impedance of the cell, P is the power delivered to the load, and Q_0 is the capacity of the battery. From Eq. 14, the maximum energy and power capability for the ideal ESD can also be determined and is given by

$$E_{max} = Q_0 U_0 \quad [16]$$

$$P_{max} = \frac{U_0^2}{4R_s} \quad [17]$$

Batteries, however, show strong nonlinear behavior and are strongly dependent on properties such as ohmic impedance (e.g., electrolyte conductivity, electronic contacts, etc.), ionic impedance, electrode thickness, and temperature, etc.[35] For ESD, these properties can more accurately be mapped from impedance data to model the power and energy density relationship. From the equivalent circuit in Fig. 9, which was mapped from impedance data in the frequency domain to the time domain, the energy and power density at the load can be defined by

$$P = \frac{1}{m\tau}\int_0^\tau U(t)i(t)dt \quad [18]$$

$$E = \int_0^\tau P(t)dt \quad [19]$$

where m is the mass of the energy storage device, τ is the discharge time duration, $U(t)$ is the time-dependent load voltage, and $i(t)$ is the time-varying current, which is dependent on

$$i(t) = \frac{P(t)}{U(t)} \quad [20]$$

In order to evaluate the power and energy capabilities of Sony UP383562A LIP battery, Eq. 18 and 19 were integrated into the equivalent circuit model of our battery (Fig. 9). Simulation started at a maximum voltage of 4.15 V (fully charged), and then discharged to a cutoff voltage of 3.0 V using constant power discharge (i.e., the power is held constant by continuously adjusting the voltage and current). At the end of discharge, the specific energy was determined using Eq. 18. To generate the Ragone plot from simulation, the simulations in the previous step were repeated using constant power discharge in the range of 0.5–22 W.

Figure 13 shows a Ragone plot (specific energy vs specific power), which was generated from the experimental and simulated data for cell UP383562A. From this plot, key observations are made. Our simulation indicates that this cell can achieve a maximum energy density of ~171 Wh/kg compared to the experimental value of 167 Wh/g. To determine the Ragone plot experimentally, the cell was discharged from the fully charged state (4.15 V) for a minimum discharge potential (3.0 V) using constant power discharge protocol. The predicted maximum deliverable specific power obtained from simulation was ~500 W/kg.

Conclusion

A generalized impedance-based model, which takes into account nonhomogeneous battery dynamics, has been developed using nonlinear lumped elements. Experimental results have demonstrated that the equivalent circuit in Fig. 4 can accurately be used to model the dynamic and transient response of lithium-ion polymer batteries. The equivalent circuit model was obtained by collecting impedance data over a range of frequencies and SOC, and then the method of NLLS fitting was used for the optimization of circuit parameters. The charge transfer resistance R_{CT} was the only parameter observed to be a function of both SOC and current magnitude and direction. This relationship can be elucidated by conducting EIS analysis using a constant dc current with a small sinusoidal stimulus current superimposed. The time-domain model can then be developed from the frequency response, which can adequately model the nonlinear performance during pulse charge–discharge sequence and constant dc charge–discharge current. The terminal voltage can be described well, theoretically, over a wide range of potentials. The experimental results showed that computer simulation can be useful in understanding real-time battery performance, which can result in reduced cost and accelerated design cycles, optimization of battery software, and hardware control for diverse applications. Additionally, components of this model include accurately modeling battery run time and correctly predicting the overall trend in specific energy vs specific power densities (Ragone plot). It has also been shown that computer simulation can also be useful when device capability is limited (i.e., the ESD in this experiment had a limited maximum discharge current); however, simulation does not have this limitation, which allows the projection of power vs energy at higher discharge rates.

Acknowledgments

This work was partially supported by U.S. Army CERDEC and National Science Foundation ERC Program.

Florida A&M University and Florida State University assisted in meeting the publication costs of this article.

References

1. L. J. Fu, H. Liu, C. Li, Y. P. Wu, E. Rahm, R. Holze, and H. Q. Wu, *Solid State Sci.*, **8**, 113 (2006).
2. Y. F. Chen and J. W. Evans, *J. Electrochem. Soc.*, **141**, 2947 (1994).
3. M. Doyle, J. P. Meyers, and J. Newman, *J. Electrochem. Soc.*, **147**, 99 (2000).
4. M. S. Wu, P. C. J. Chiang, and J. C. Lin, *J. Electrochem. Soc.*, **152**, A47 (2005).
5. D. P. Abraham, J. L. Knuth, D. W. Dees, I. Bloom, and J. P. Christophersen, *J. Power Sources*, **170**, 465 (2007).
6. K. Takano, K. Nozaki, Y. Saito, A. Negishi, K. Kato, and Y. Yamaguchi, *J. Power Sources*, **90**, 214 (2000).
7. G. Ning, R. E. White, and B. N. Popov, *Electrochim. Acta*, **51**, 2012 (2006).
8. M. Doyle, J. Newman, A. S. Gozdz, C. N. Schmutz, and J. M. Tarascon, *J. Electrochem. Soc.*, **143**, 1890 (1996).
9. E. Kuhn, C. Forgez, and G. Friedrich, *Eur. Phys. J.: Appl. Phys.*, **25**, 183 (2004).
10. S. Buller, M. Thele, R. W. A. A. De Doncker, and E. Karden, *IEEE Trans. Ind. Appl.*, **41**, 742 (2005).
11. P. L. Moss, J. P. Zheng, G. Au, P. J. Cygan, and E. J. Plichta, *J. Electrochem. Soc.*, **154**, A1020 (2007).
12. R. W. J. M. Huang, F. Chung, and E. M. Kelder, *J. Electrochem. Soc.*, **153**, A1459 (2006).
13. S. Rodrigues, N. Munichandraiah, and A. K. Shukla, *J. Power Sources*, **87**, 12 (2000).
14. K. Dokko, Y. Fujita, M. Mohamedi, M. Umeda, I. Uchida, and J. R. Selman, *Electrochim. Acta*, **47**, 933 (2001).
15. C. H. Chen, J. Liu, and K. Amine, *J. Power Sources*, **96**, 321 (2001).
16. M. Mohamedi, D. Takahashi, T. Uchiyama, T. Itoh, M. Nishizawa, and I. Uchida, *J. Power Sources*, **93**, 93 (2001).
17. S. H. Chan, K. A. Khor, and Z. T. Xia, *J. Power Sources*, **93**, 130 (2001).
18. D. Zhang, B. N. Popov, and R. E. White, *J. Electrochem. Soc.*, **147**, 831 (2000).
19. H. B. Oldham and J. C. Myland, *Fundamental of Electrochemical Science*, p. 474, Academic Press, New York (1994).
20. S. Buller, M. Thele, E. Karden, and R. W. De Doncker, *J. Power Sources*, **113**, 422 (2003).
21. B. E. Conway, *Electrochemical Supercapacitor: Scientific Fundamental and Technology Applications*, p. 698, Kluwer Academic/Plenum Publisher, New York (1999).

22. D. D. Macdonald, *Electrochim. Acta*, **51**, 1376 (2006).
23. M. D. Levi, Z. Lu, and D. Aurbach, *Solid State Ionics*, **143**, 309 (2001).
24. E. Karden, S. Buller, and R. W. De Doncker, *Electrochim. Acta*, **47**, 2347 (2002).
25. M. D. Levi, K. Gamolsky, D. Aurbach, U. Heider, and R. Oesten, *Electrochim. Acta*, **45**, 1781 (2000).
26. O. E. Barcia, E. D'Elia, I. Frateur, O. R. Mattos, N. Pebere, and B. Tribollet, *Electrochim. Acta*, **47**, 2109 (2002).
27. P. Mauracher and E. Karden, *J. Power Sources*, **67**, 69 (1997).
28. H. Li, X. J. Huang, and L. Q. Chen, *J. Power Sources*, **82**, 340 (1999).
29. J. S. Kim and Y. T. Park, *J. Power Sources*, **91**, 172 (2000).
30. N. Cui and J. L. Luo, *Electrochim. Acta*, **45**, 3973 (2000).
31. G. Lijun, L. Shengyi, and R. A. Dougal, *IEEE Trans. Compon., Packag. Manuf. Technol., Part A*, **25**, 495 (2002).
32. S. Piller, M. Perrin, and A. Jossen, *J. Power Sources*, **96**, 113 (2001).
33. T. Christen and M. W. Carlen, *J. Power Sources*, **91**, 210 (2000).
34. E. Barsoukov, J. H. Kim, C. O. Yoon, and H. Lee, *J. Power Sources*, **83**, 61 (1999).
35. M. Doyle and Y. Fuentes, *J. Electrochem. Soc.*, **150**, A706 (2003).